Available online at www.sciencedirect.com
ScienceDirect
Journal of the European Ceramic Society 28 (2008) 811–820
www.elsevier.com/locate/jeurceramsoc

Influence of sintering conditions on microstructure and electrical conductivity of yttrium-substituted $SrTiO_3$

Q.X. Fu [a], S.B. Mi [b], E. Wessel [a], F. Tietz [a,*]

[a] *Institut für Energieforschung (IEF), Forschungszentrum Jülich GmbH, 52425 Jülich, Germany*
[b] *Institut für Festkörperforschung (IFF), Forschungszentrum Jülich GmbH, 52425 Jülich, Germany*

Received 11 November 2006; received in revised form 19 July 2007; accepted 27 July 2007
Available online 17 October 2007

Abstract

The microstructure and electrical conductivity of Y-substituted $SrTiO_3$ ceramics ($Sr_{1-\alpha x}Y_xTiO_{3-\delta}$, $x = 0$, 0.035, 0.07; $\alpha = 1.0$, 1.5) sintered under both oxidizing and reducing conditions were studied in detail. In these compositions, Y^{3+} ions have been found to occupy the Sr sites and act as donor substitutes. The observed interesting dependence of the microstructure and electrical property on the starting composition (cation nonstoichiometry) and the sintering or processing conditions indicates that the defect chemistry known for other donor-substituted $SrTiO_3$ (e.g. $Sr_{1-x}La_xTiO_{3-\delta}$) ceramics also applies for Y-substituted $SrTiO_3$ ceramics. The positive charge from the Y-substitute can be compensated either electronically under reducing conditions or ionically under oxidizing conditions. Therefore, to obtain a single-phase and highly conductive yttrium-substituted $SrTiO_3$ material, e.g. as a candidate for an SOFC anode, a starting composition with (Sr + Y)/Ti = 1 and a high-temperature heat treatment (>1200 °C) under reducing conditions is required.

Keywords: Perovskites; $SrTiO_3$; Microstructure; Electrical conductivity; Defect chemistry

1. Introduction

Alternative materials are required in order to overcome problems with state-of-the-art Ni-based anode materials for solid oxide fuel cells (SOFCs), such as coking[1] and volume instability upon cyclic reduction–oxidation (redox cycling).[2] Donor-substituted $SrTiO_3$ ceramics are considered to be promising candidate materials due to their good chemical stability and relatively high *n*-type electronic conductivity under reducing conditions. For instance, $La_xSr_{1-x}TiO_3$ materials have been shown by Marina et al.[3] to have good dimensional stability upon redox cycling as well as good electronic conductivity in fuel gas atmosphere although their electrochemical performance is poor. Recently, Hui and Petric[4] measured unusually high electrical conductivity for yttrium-substituted $SrTiO_3$ (SYT) as compared to those with rare-earth substitutes (e.g. La, Pr, Sm, Gd, Yb). The composition $Sr_{0.88}Y_{0.08}TiO_3$ shows a conductivity of 64 S/cm at 800 °C and oxygen partial pressure ($p(O_2)$) of 10^{-19} bar. More detailed studies of this material are, therefore, desirable.

Previous studies on the defect chemistry of donor-substituted $SrTiO_3$ or $BaTiO_3$ materials (with La^{3+} and Nb^{5+} as typical donor substituents) have concluded that the charge compensation mode (either ionically or electronically) depends strongly on the $p(O_2)$. Consequently, the change of charge compensation mode upon the change of $p(O_2)$ dictates a change of A/B ratio in the perovskite lattice (ABO_3), necessitating the segregation or absorption of a second phase, as observed with La- or Nb-substituted $BaTiO_3$ ceramics.[5,6] Furthermore, the sintering atmosphere significantly affects the electrical property. For instance, under typical SOFC anode conditions, $La_xSr_{1-x}TiO_3$ ceramics ($x = 0.1$–0.4) sintered in air exhibited an electrical conductivity in the order of 1–16 S/cm, whereas those materials sintered in hydrogen at 1650 °C showed 80–360 S/cm.[3] The phase formation and electrical property of Y-substituted $SrTiO_3$ ceramics as a function of sintering atmosphere, however, have not been addressed in the previous study.[4]

In the present work, Y-substituted $SrTiO_3$ ceramics with various starting compositions have been synthesized and sintered under both oxidizing and reducing conditions. Their phase evo-

* Corresponding author. Tel.: +49 2461 615007; fax: +49 2461 612455.
E-mail address: f.tietz@fz-juelich.de (F. Tietz).

0955-2219/$ – see front matter © 2007 Elsevier Ltd. All rights reserved.
doi:10.1016/j.jeurceramsoc.2007.07.022

lution, microstructure and electrical conductivity have then been studied in detail.

2. Experimental

As the solubility of Y in $SrTiO_3$ with the formula $Sr_{1-1.5x}Y_xTiO_{3-\delta}$ was reported to be 8 at.%,[4] the Y content in the present study was chosen as 0, 3.5 and 7 at.%. For each Y content, both stoichiometric ($Sr_{1-x}Y_xTiO_{3-\delta}$) and A-site deficient ($Sr_{1-1.5x}Y_xTiO_{3-\delta}$) compositions were prepared. Abbreviations for all compositions studied are listed in Table 1.

The Pechini method[7] was used for the powder synthesis. Strontium nitrate (p.a. [>99.0%], Merck), yttrium nitrate hexahydrate (99.9%, Alfa Aesar) and titanium isopropoxide (>97%, Alfa Aesar) were used as the starting chemicals. To control the final compositions as precisely as possible, the hygroscopic nitrates were first dissolved in water, and then assayed by the thermogravimetric method. Titanium isopropoxide was dissolved in ethylene glycol and citric acid to form a stable solution that can be readily mixed with other aqueous nitrate solutions without causing precipitation. The Ti content in the as-prepared Ti solution was also assayed by the thermogravimetric method. During the concentrating process of the precursor solution, no precipitate or turbidity was observed, indicating near-molecular-level cation mixing throughout the whole process. The resulting resins were then calcined at 900 °C for 5 h in air to completely burn out the organic substances and obtain the primary powders. The primary powders were uniaxially pressed into rectangular bars (3 mm × 5 mm × 40 mm) and then sintered either in air or Ar/4% H_2 at 1300–1400 °C for 10 h. Some air-sintered samples were reduced in Ar/4% H_2 at 1000–1300 °C for 10 h. The heating and cooling rate was 3 and 5 °C/min, respectively. The $p(O_2)$ of Ar/4% H_2 (with a certain but unknown humidity) used for the present study is about 10^{-22} bar at 800 °C as determined by a zirconia oxygen sensor.

The phase formation and microstructure of the samples were studied by powder X-ray diffraction (XRD, Siemens D5000, Cu Kα radiation) and scanning electron microscopy (SEM, LEO Gemini 1530) in combination with energy-dispersive X-ray spectroscopy (EDS). Lattice parameters were fitted with the related software including PowderX[8] and Dicvol91.[9]

SYT70b samples showed an apparent Ti-rich secondary phase after sintering in Ar/4% H_2 at 1400 °C for 10 h. The composition and structure of this Ti-rich phase was analyzed using wavelength-dispersive X-ray spectroscopy (WDS) and transmission electron microscopy (TEM, Philips CM20-FEG) in combination with selected area electron diffraction (SAED). Due to the energy overlap of the X-ray lines of Y and Sr and the relatively low content of Y in this composition, EDS cannot be used to determine the composition with good accuracy. The specimens for TEM investigations were prepared by cutting discs with a diameter of 3 mm from the ceramic bodies using an ultrasonic cutter. The discs were then ground, dimpled and finally thinned to perforation by ion-milling on a stage cooled by liquid nitrogen. The transmission electron microscope was operated at 200 kV.

The electrical conductivity was measured by the DC four-probe method at 25–910 °C in either air or wet Ar/4% H_2. Gas humidification was performed by passing the gas through a water container at ambient temperatures (20–25 °C). The resulting gas containing 2.3–3.1% of water vapour is termed here "wet" gas ($\log p(O_2)/\text{bar} = -18.7 \pm 0.1$ for wet Ar/4% H_2 at 800 °C).

Table 1
Nominal compositions and abbreviations of $Sr_{1-\alpha x}Y_xTiO_{3-\delta}$ ceramics investigated in this study

x	Stoichiometric $\alpha = 1$	A-site deficient $\alpha = 1.5$
0	$SrTiO_{3-\delta}$ (ST)	
0.035	$Sr_{0.965}Y_{0.035}TiO_{3-\delta}$ (SYT35a)	$Sr_{0.9475}Y_{0.035}TiO_{3-\delta}$ (SYT35b)
0.070	$Sr_{0.93}Y_{0.07}TiO_{3-\delta}$ (SYT70a)	$Sr_{0.895}Y_{0.07}TiO_{3-\delta}$ (SYT70b)

3. Results

3.1. Phase development and microstructure

XRD patterns of $Sr_{1-\alpha x}Y_xTiO_{3-\delta}$ sintered in air at 1400 °C for 10 h are shown in Fig. 1. For the stoichiometric compositions ($\alpha = 1$), a secondary phase ($Y_2Ti_2O_7$) was observed even for the composition with only 3.5 at.% Y. Further increasing the Y content in the starting composition (i.e. SYT70a) merely resulted in an increasing amount of $Y_2Ti_2O_7$. For the A-site deficient samples ($\alpha = 1.5$), however, single-phase powder was observed for SYT35b. For the SYT70b composition in the present work, the Y content still exceeds the solubility, leading to the formation

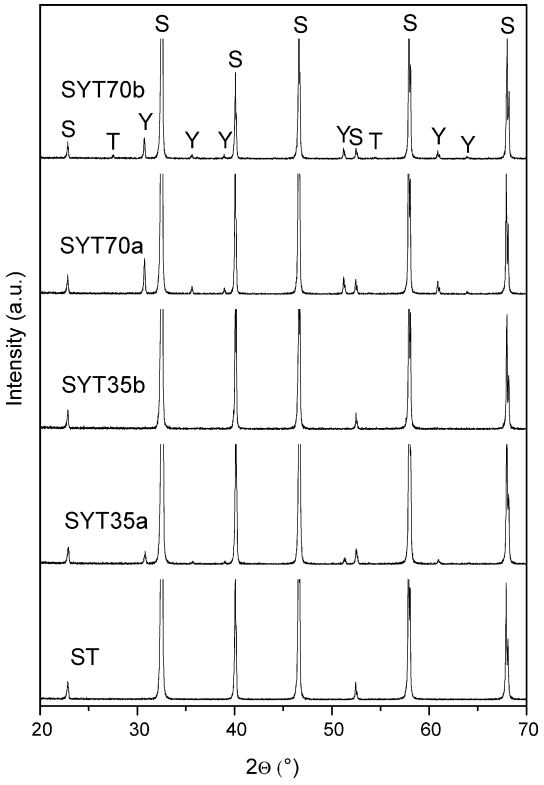

Fig. 1. XRD patterns for samples sintered in air at 1400 °C for 10 h. S: $SrTiO_3$, Y: $Y_2Ti_2O_7$, T: TiO_2.

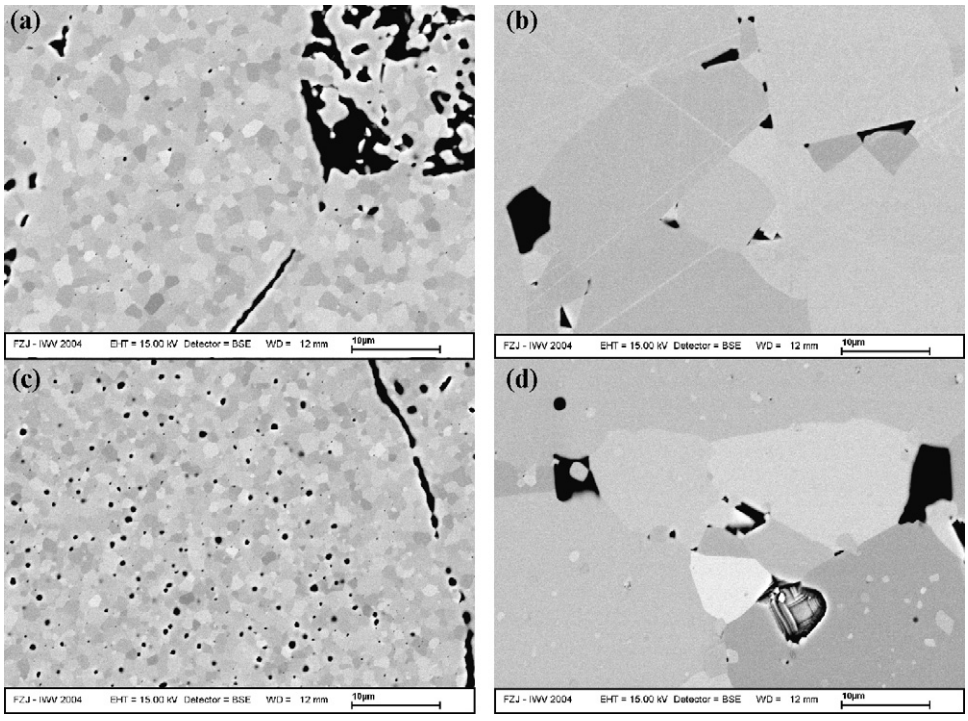

Fig. 2. Microstructure of SYT samples sintered in air at 1400 °C for 10 h. (a) SYT35a; (b) SYT35b; (c) SYT70a; (d) SYT70b (10 μm scale bar). In back-scattering mode, the SEM images show different gray scales for various crystallite orientations of the grains.

of $Y_2Ti_2O_7$. In addition, TiO_2 was also observed as another minor impurity.

The stoichiometry of the starting composition significantly affects the microstructure of air-sintered samples, as shown in Fig. 2. The A-site deficient compositions (SYT35b and SYT70b) show enhanced grain growth with a particle size of 30–40 μm, while the stoichiometric compositions (SYT35a and SYT70a) show uniform fine-grained microstructures (particle size 2–3 μm). The relative density of SYT35b or SYT70b (95–97%) is also about 10% higher than that of SYT35a or SYT70a (85–87%).

For samples sintered in Ar/4% H_2 at 1400 °C for 10 h, the XRD results indicated pure perovskites for all compositions (Fig. 3), except SYT70b which showed a few weak peaks of a secondary phase. However, this phase is difficult to identify from the XRD results due to its very low diffraction intensity. Therefore, microanalysis using SEM (in combination with EDS and WDS) and TEM was carried out. SEM images for both SYT70a and SYT70b are shown in Fig. 4. While SYT70a showed a homogeneous structure as also confirmed by multipoint EDS analysis, SYT70b apparently contained a Ti-rich phase. To determine the elemental composition more accurately, WDS analysis was performed on both phases in SYT70b sintered at 1400 °C, with four points randomly detected for each phase. The major phase had a composition of $Sr_{0.93\pm0.02}Y_{0.066\pm0.002}TiO_{3-\delta}$, and the secondary phase $SrTi_{10.7\pm0.2}O_{23-\delta}$. No Y could be detected in the secondary phase within the experimental limit of WDS. Therefore, in spite of the starting composition, a ratio of (Sr + Y)/Ti = 1 was observed in the perovskite phase of SYT70b.

Under reducing conditions, no increased grain growth was observed. Samples sintered at 1300 °C showed smaller grain size

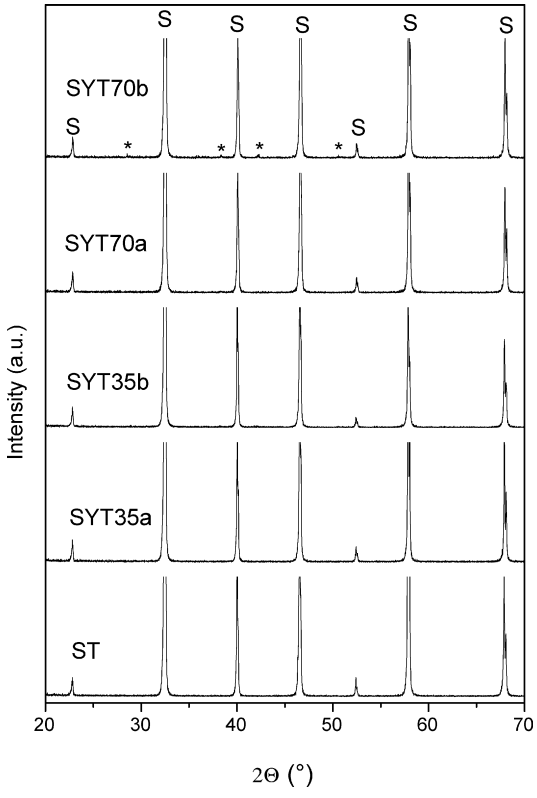

Fig. 3. XRD patterns for samples sintered in Ar/4% H_2 at 1400 °C for 10 h. S: $SrTiO_3$, asterisk (*): unknown Ti-rich phase.

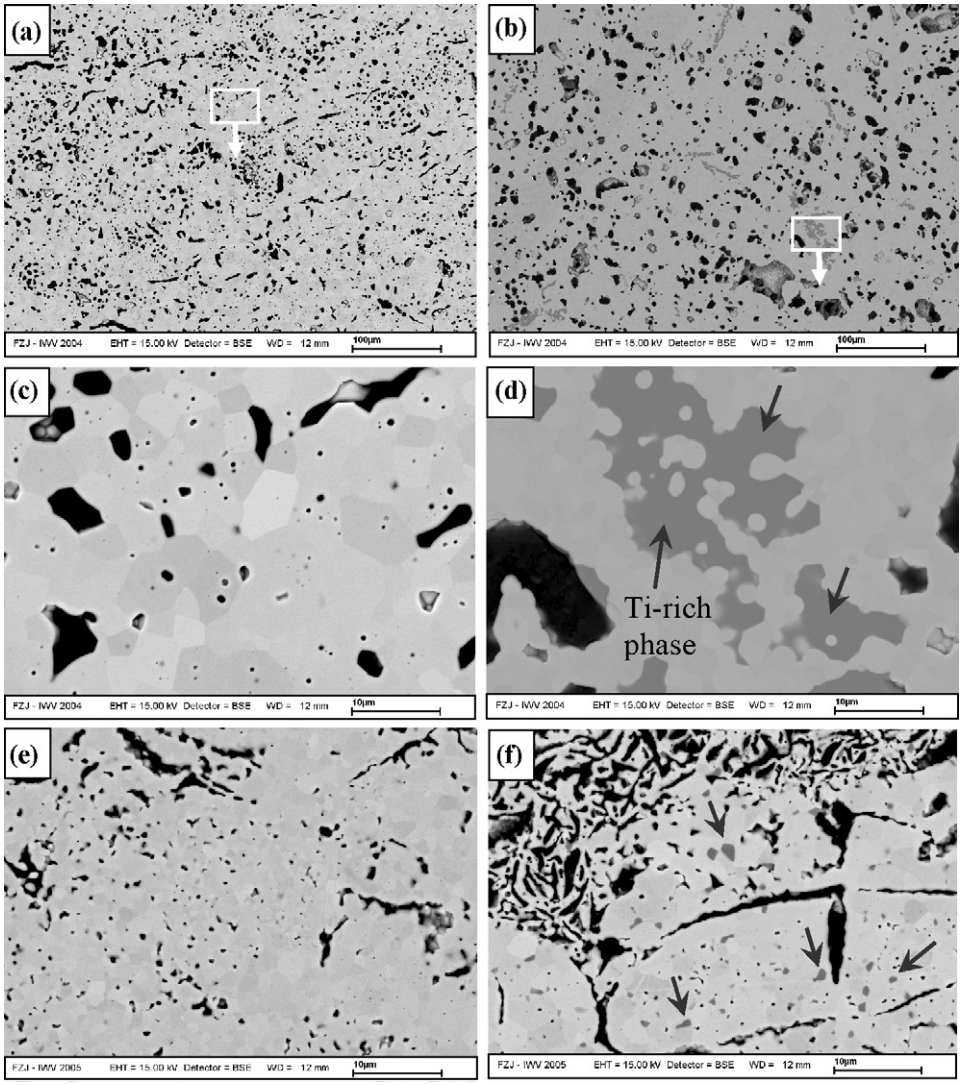

Fig. 4. Microstructure of SYT70a (a, c and e) and SYT70b (b, d and f) sintered in Ar/4% H_2 at 1400 °C (a, b, c and d) or 1300 °C (e and f) for 10 h (c and d) are enlarged views of framed areas in (a and b), respectively. The Ti-rich phases in (d and f) can be distinguished by the contrast and are indicated by arrows. Scale bars represent 100 μm in (a and b) and 10 μm in (c–f).

(1–3 μm) than those sintered at 1400 °C (3–6 μm) (Fig. 4). In addition, the amount of the segregated Ti-rich phase in SYT70b sintered at 1300 °C is much smaller than at 1400 °C. A Ti-rich phase was also observed in the reduced SYT35b with SEM, but in much smaller quantities than in SYT70b, which is in accordance with the clean XRD pattern showing only the perovskite of SYT35b.

TEM investigation was performed to clarify the structure of the Ti-rich secondary phase in the reduced SYT70b (Fig. 5). The cubic perovskite structure of the major phase was confirmed by SAED, in agreement with the XRD results. SAED patterns of the Ti-rich secondary phase, however, gave insufficient information to create a three-dimensional construction of this phase. From the SAED pattern along one direction one interplanar distance of about 0.74 nm was determined indicating that its unit cell is much larger than that of the major phase. In the literature, two phases were reported with chemical compositions quite close to that was observed in the present work. In the Sr–Ti–O phase diagram studied on ceramics at 1350 °C, McCarthy et al.[10] observed a Ti-rich phase, tentatively identified as "$SrTi_{12}O_{19}$". The reported XRD pattern for "$SrTi_{12}O_{19}$", however, is completely different from what has been observed for the Ti-rich phase in the reduced SYT70b sample. Another reduced Sr–Ti–O compound, $SrTi_{11}O_{20}$, in the form of small single crystals was first prepared by Hessen et al.[11] It has a triclinic structure with space group $P\bar{1}$ ($a = 0.71252(8)$ nm, $b = 0.76644(8)$ nm, $c = 1.3157(2)$ nm, $\alpha = 90.21(1)^\circ$, $\beta = 92.79(1)^\circ$ and $\gamma = 103.94(1)^\circ$). Attempts to index the obtained SAED data with the lattice parameters of $SrTi_{11}O_{20}$ were not successful. Therefore, it is considered that a new phase in the Sr–Ti–O system was formed under the specific sintering conditions used in the present work.

As shown in Fig. 6, the lattice parameters of the SYT perovskite phase under both sintering conditions decrease with increasing Y content down to the solubility limit. Under oxidizing conditions, the solubility of Y in $SrTiO_3$ depends significantly on the A-site stoichiometry. Its limit is estimated to

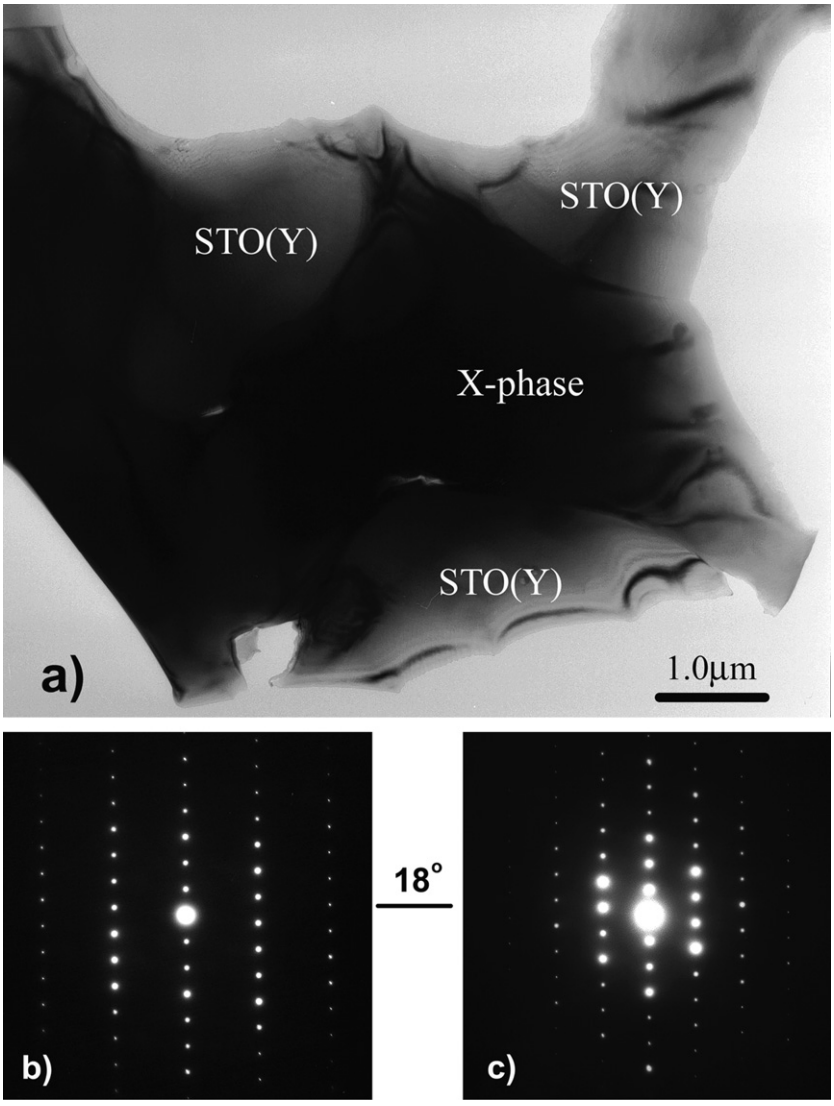

Fig. 5. TEM bright-field image of SYT70b sintered in Ar/4% H_2 at 1400 °C for 10 h (a), showing the major perovskite phase (marked as STO(Y) on the picture) and the secondary Ti-rich phase with unknown structure (X-phase). SAED patterns of the X-phase are shown in (b and c).

be 1 and 4 at.% with stoichiometric and A-site deficient starting composition, respectively. Under reducing conditions, it seems that A-site deficiency in the starting composition only leads to the segregation of the Ti-rich secondary phase, and would have no significant impact on Y solubility in the major phase. Y solubility in $SrTiO_3$ under reducing conditions is about 8 at.%, which is in agreement with the previous results.[4] However, in contrast to the present work, no dependence of the Y solubility on the sintering atmosphere was mentioned.[4]

3.2. Electrical conductivity

The electrical conductivity of air-sintered samples was first measured in air, and then in wet Ar/4% H_2. Stable isothermal conductivity was observed when measured in air, i.e. the electrical conductivity did not change with time when the temperature was kept constant. The conductivity of all compositions studied is shown in Fig. 7. The electrical conductivity of pure $SrTiO_3$ is $\sim 10^{-3}$ S/cm at 850 °C, and the apparent activation energy is 1.52 ± 0.03 eV, both being in good agreement with the results reported by Balachandran and Eror.[13] For the Y-substituted samples, the conductivities of the stoichiometric compositions (SYT35a and SYT70a) are nearly identical and are lower than that of pure $SrTiO_3$ below 900 °C. The A-site deficient compositions (SYT35b and SYT70b) also show nearly identical conductivities, which are, however, 2–4 orders of magnitude higher than that of $SrTiO_3$.

Time-dependent isothermal conductivity was observed when measuring the air-sintered samples in wet Ar/4% H_2 (Fig. 8). During the measurement, the samples were reduced in wet Ar/4% H_2 at 910 °C for 15 h before cooling down. In comparison with the data in air (Fig. 7), the reduction process led to a rapid increase of conductivity for SYT35a and SYT70a by almost three orders of magnitude to nearly 1 S/cm at 910 °C, whereas no significant increase was observed for SYT35b and SYT70b. In addition, the increase of conductivity did not reach

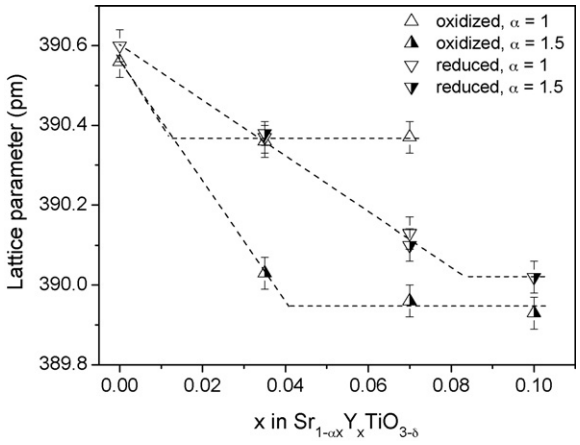

Fig. 6. Lattice parameter of the cubic perovskite phase in both oxidized and reduced $Sr_{1-\alpha x}Y_xTiO_{3-\delta}$ ($\alpha = 1$, stoichiometric; $\alpha = 1.5$, A-site deficient) samples as a function of nominal yttrium content, x. Data for $x = 0.10$ and $\alpha = 1.5$ ($Sr_{0.85}Y_{0.10}TiO_{3-\delta}$) were deduced from the results of our previous work.[12] Oxidized and reduced samples were obtained by sintering at 1400 °C for 10 h in air and in Ar/4% H_2, respectively.

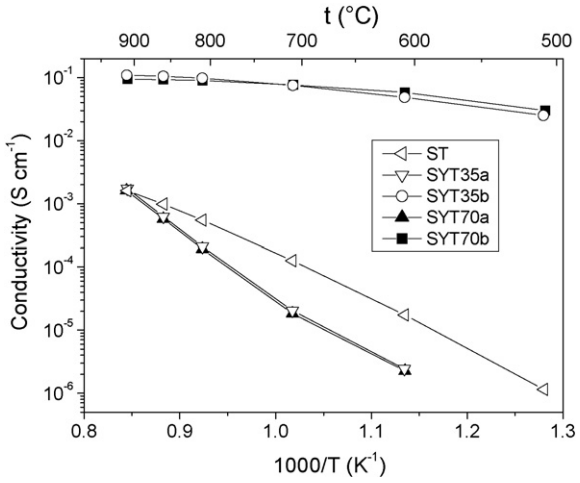

Fig. 7. Temperature dependence of the electrical conductivity in air for samples sintered in air at 1400 °C for 10 h.

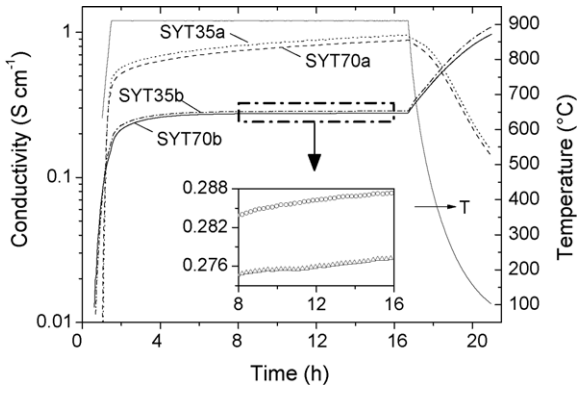

Fig. 8. Time and temperature dependence of the electrical conductivity in wet Ar/4% H_2 for samples sintered in air at 1400 °C for 10 h.

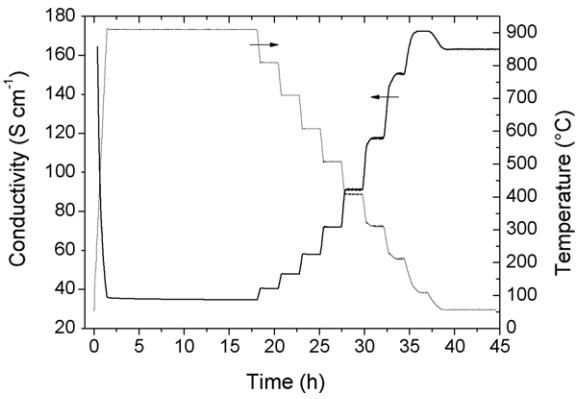

Fig. 9. Typical conductivity measurement run for samples sintered in Ar/4% H_2 and measured in wet Ar/4% H_2. The sample shown in this figure is SYT35a sintered at 1400 °C for 10 h.

equilibrium after 15 h and the rate of increase for SYT35b and SYT70b was much slower than that for SYT35a and SYT70a (inset of Fig. 8).

The electrical conductivity of H_2-sintered samples was directly measured in wet Ar/4% H_2. A typical measurement run is shown in Fig. 9. During the measurement, the samples were kept at 910 °C for 15 h before cooling down in steps of 100 °C. It seems that stable conductivity values were obtained within the time scale of these measurements. Fig. 10 shows the temperature dependence of the as-measured electrical conductivity for samples sintered in Ar/4% H_2 at 1400 °C for 10 h. Compared with samples sintered in air (Fig. 8), those sintered in Ar/4% H_2 show much higher electrical conductivity in wet Ar/4% H_2. For instance, air-sintered SYT70a shows a conductivity of less than 1 S/cm even after 15 h of reduction at 910 °C in wet Ar/4% H_2, whereas H_2-sintered SYT70a shows a conductivity of 70 S/cm under the same measurement conditions. By re-plotting the data in Fig. 10, a linear relationship between the yttrium content and the electrical conductivity of $Sr_{1-x}Y_xTiO_{3-\delta}$ was observed, as shown in Fig. 11.

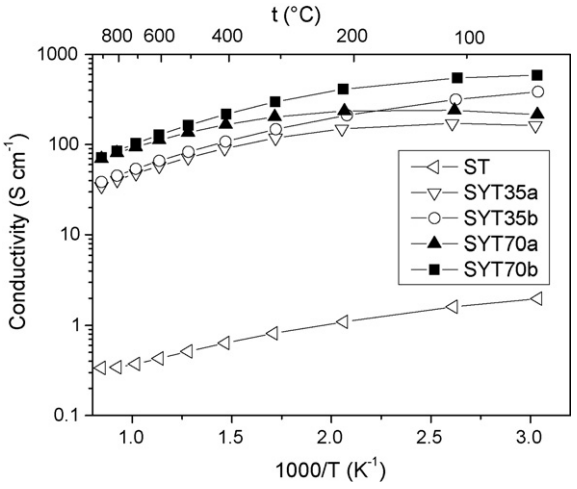

Fig. 10. Temperature dependence of the as-measured electrical conductivity in wet Ar/4% H_2 for samples sintered in Ar/4% H_2 at 1400 °C for 10 h. Data were obtained using the measurement procedure shown in Fig. 9.

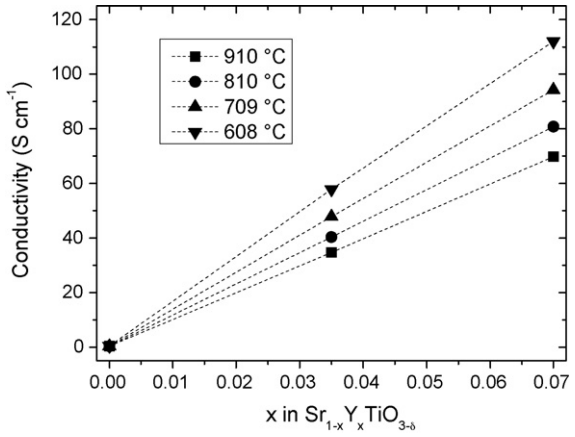

Fig. 11. Linear dependence of the electrical conductivity of $Sr_{1-x}Y_xTiO_{3-\delta}$ on the yttrium content at different temperatures (data taken from Fig. 10). Samples were sintered in Ar/4% H_2 at 1400 °C for 10 h and measured in wet Ar/4% H_2 at temperatures lower than 910 °C.

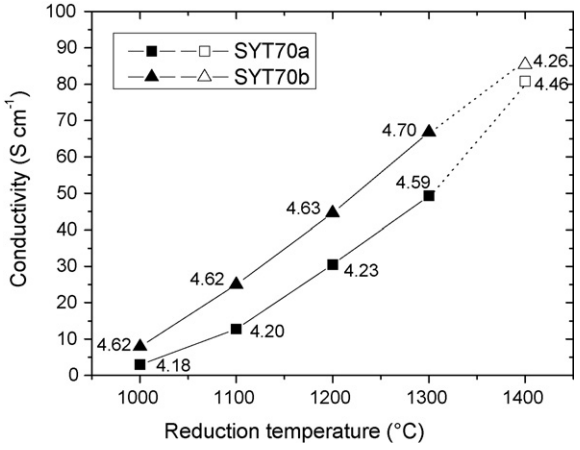

Fig. 12. Influence of the reduction temperature on the electrical conductivity (at 810 °C and in wet Ar/4% H_2) of SYT70a and SYT70b samples that had experienced a high-temperature reduction process. Closed symbols indicate samples sintered in air at 1300 °C for 10 h and then reduced in Ar/4% H_2 at different temperatures for 10 h. Open symbols indicate samples sintered directly in Ar/4% H_2 at 1400 °C. Numbers besides each symbol indicate the sample density in g/cm^3.

For the air-sintered samples, a high-temperature post-reduction process can significantly improve the electrical conductivity. As shown in Fig. 12, the electrical conductivity of the post-reduced air-sintered SYT70a and SYT70b samples increases with the reduction temperature (the reduction time was fixed at 10 h).

4. Discussion

4.1. Defect chemistry of donor-substituted $SrTiO_3$

The defect chemistry of SYT is determined by the site occupancy of Y^{3+} in $SrTiO_3$. Previous work[14–18] has revealed an amphoteric behavior of Y^{3+} in $BaTiO_3$ due to its intermediate ionic radius between those of Ba^{2+} and Ti^{4+}.[19] Depending on the starting composition (Ba/Ti ratio), Y^{3+} can occupy either Ba or Ti sites. Similar behavior is expected for the incorporation

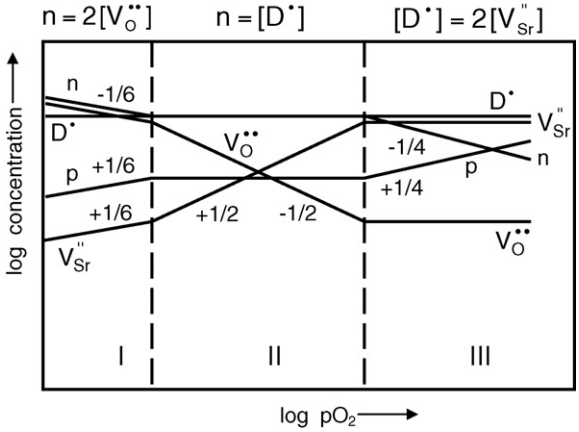

Fig. 13. Kröger–Vink diagram for donor-substituted $SrTiO_3$.

of Y^{3+} in the $SrTiO_3$ structure, i.e. with $(Y + Sr)/Ti \leq 1$ in the starting compositions, Y^{3+} ions are expected to preferentially occupy the Sr sites, acting as donors. This is confirmed by the smaller lattice constants of the solid solution compared with that of the pure $SrTiO_3$, as shown in Fig. 6 in the present work and as reported previously.[4]

The defect chemistry of donor-substituted $SrTiO_3$ (with La^{3+} as a typical donor substituent) has been studied extensively in the literature.[20–24] A Kröger–Vink diagram as shown in Fig. 13 is generally accepted to illustrate the variation of the defect concentrations as a function of $p(O_2)$ for donor-substituted $SrTiO_3$. The donor substituent, D, is assumed to be fully ionized, $D^{\bullet}$. The extra positive charge of the donor has to be compensated to maintain electroneutrality.

(i) Under oxidizing conditions (region III in Fig. 13), it is compensated ionically by strontium vacancies. Using the Kröger–Vink[25] notation, the electroneutrality condition (ENC) can be expressed by

$$[D^{\bullet}] = 2[V''_{Sr}] \quad (1)$$

The perovskite phase of SYT is then Sr-deficient and can be represented by $Sr_{1-3z/2}\square_{z/2}Y_zTi^{4+}O_3$ ("□" represents a vacant Sr site). The electrical conductivity is low due to the lack of Ti^{3+}.

(ii) Under moderate reducing conditions (region II), it is compensated electronically by the reduction of Ti^{4+} to Ti^{3+}, generating equal numbers of conduction electrons. The ENC is then

$$n = [D^{\bullet}] \quad (2)$$

Accordingly, the perovskite phase of SYT has an equal number of A- and B-site occupancies ($(Sr + Y)/Ti = 1$) and can be represented by $Sr_{1-z}Y_zTi_{1-z}{}^{4+}Ti_z{}^{3+}O_3$. The charge carrier density, and hence the electrical conductivity, is proportional to the donor content.

(iii) Under strongly reducing conditions (region I), donor-type oxygen vacancies are the predominant ionic defects. They

are counterbalanced by conduction electrons according to

$$n = 2[V_O^{\bullet\bullet}] \quad (3)$$

The perovskite phase of SYT still has an equal number of A- and B-site occupancies but has a significant amount of oxygen deficiency. It can be represented by $Sr_{1-z}Y_zTi_{1-z}{}^{4+}Ti_{z+2\delta}{}^{3+}O_{3-\delta}$ ($\delta \gg z$). The electrical conductivity is mainly determined by the oxygen deficiency.

4.2. Considerations on the kinetics of defect equilibration

The defect concentrations as shown in Fig. 13 are based on thermodynamic equilibrium states. Any change of $p(O_2)$ and temperature dictates the establishment of a new equilibrium state. In many cases, however, the equilibrium restoration upon change of $p(O_2)$ and temperature can not be completed within reasonable measuring times due to the limitation of ion diffusion kinetics in the solid state, as discussed extensively in previous studies of donor-substituted $BaTiO_3$.[26–30]

For SYT ceramics, the equilibrium restoration involves both cation (e.g. Sr^{2+}) and anion (O^{2-}) diffusion. The cation diffusion in a solid ceramic is known to be extremely slow (e.g. in La-doped $BaTiO_3$ the chemical diffusivity of Ba and Ti ions is about 10^{-13} to 10^{-20} cm^2/s at 900 °C [26,31–33]) and the equilibrium in the cation sublattice can only be attained at elevated temperatures near the sintering temperature. In La-substituted $SrTiO_3$, temperatures of at least 1150 °C are necessary to ensure complete equilibrium restoration in the cation sublattice within 20 h after a rapid change in temperature.[23] The oxygen diffusion is much faster in comparison to the cation diffusion. Nevertheless, since the oxygen vacancy concentration is strongly suppressed by the donor incorporation, oxygen diffusion in donor-substituted titanates is accordingly much slower than in acceptor-substituted or pure alkaline-earth titanates. As an example, the oxygen tracer diffusivity in La-substituted $SrTiO_3$ is three to five orders of magnitude lower than that in acceptor-substituted or pure $SrTiO_3$.[34,35]

Therefore, for a donor-substituted $SrTiO_3$ material, while the concentration of cationic defects (e.g. strontium vacancies) is defined by the high-temperature processing (e.g. sintering) and remains constant (frozen-in) at lower temperatures, the concentration of the anionic defects (oxygen vacancies) remains variable and may not reach equilibrium within reasonable measuring times due to the slow oxide ion diffusion at typical measuring temperatures (700–1000 °C).

4.3. Interpretation of the experimental results

In this section, the defect chemistry of donor-substituted $SrTiO_3$ as described above is used to explain the experimental results.

4.3.1. Ionic compensation for air-sintered SYT

Sintering SYT under oxidizing conditions leads to a charge compensation by strontium vacancies, as in the case of La in $SrTiO_3$.[24] Therefore, allowing strontium deficiencies in the starting compositions, which is in line with the compensation mechanism, will promote donor incorporation into Sr sites. This explains the observed enhanced Y solubility in the A-site deficient compositions (~4 at.%) in comparison to the stoichiometric compositions (~1 at.%), cf. Fig. 5. In fact, previous studies on air-sintered La-substituted $SrTiO_3$ ceramics gave the same result. With stoichiometric starting compositions ($La_xSr_{1-x}TiO_3$), Balachandran and Eror[36] found a solubility limit of $x = 0.4$ and the secondary phase $La_2Ti_2O_7$ was observed at $x > 0.4$. With A-site deficient starting compositions ($La_xSr_{1-3x/2}TiO_3$), however, Moos et al.[24] observed a complete solid solution of La in $SrTiO_3$. The lattice parameter of $La_xSr_{1-3x/2}TiO_3$ changes linearly with the La content, obeying Vegard's law up to the end member with $x = 2/3$ ($La_{2/3}TiO_3$).

The appearance of the minor phase TiO_2 in the air-sintered SYT70b sample can also be explained by assuming strontium vacancies as the compensating defects. As the un-dissolved Y combines with equal moles of Ti to form $Y_2Ti_2O_7$, there is a higher Sr deficiency than actually required, dictating the segregation of another Ti-rich phase (here TiO_2) according to

$$\text{“}Sr_{1-3x/2}Y_xTiO_3\text{”} \rightarrow y[Sr_{(1-3x/2)/y}\square_{(x-\alpha)/2y}Y_{(x-\alpha)/y}TiO_3] + \alpha/2Y_2Ti_2O_7 + \alpha/2TiO_2 \quad (4)$$

where $y = 1-3\alpha/2$ and "□" represents a vacant Sr site. The left side of this equation only indicates the nominal starting composition. Using the Y solubility in $Sr_{1-3x/2}Y_xTiO_3$ (4 at.%) observed in the present work, Eq. (4) can be rewritten as

$$\text{“}Sr_{0.895}Y_{0.07}TiO_3\text{”} \rightarrow 0.952Sr_{0.94}\square_{0.02}Y_{0.04}TiO_3 + 0.016Y_2Ti_2O_7 + 0.016TiO_2 \quad (4')$$

The ionic compensation for air-sintered SYT is also supported by the low electrical conductivity measured in air (Fig. 7 in comparison with Fig. 10). The observed much higher electrical conductivity for A-site deficient compositions than that of stoichiometric compositions, however, needs further explanation. It could be correlated to their unique microstructures, i.e. enhanced grain growth as compared with the stoichiometric compositions (Fig. 2) in analogy to air-sintered donor-doped $BaTiO_3$ materials,[27,37,38] which are coarse-grained semiconducting materials when the donor content is below ~0.3 at.%, whereas higher donor contents lead to fine-grained insulating materials.

Regarding the microstructural difference between the A-site deficient and stoichiometric compositions, Burn and Neirman[39] reported similar results for the air-sintered Y^{3+} and Nb^{5+}-substituted $SrTiO_3$. Dense and coarse-grained (~25 μm) materials were obtained with A-site deficient compositions, whereas poorly densified and fine-grained (1–2 μm) materials were obtained with stoichiometric compositions. There have also been extensive studies on $BaTiO_3$-based ceramics, showing the sensitivity of grain growth to cation nonstoichiometry.[40,41]

4.3.2. Electronic compensation for H_2-sintered SYT

Sintering SYT under reducing conditions leads to a charge compensation by conduction electrons. This is supported by

three facts observed in the present work:

(i) The perovskite phase in H_2-sintered SYT has an equal number of A- and B-site occupancies ((Sr + Y)/Ti = 1). Accordingly, the H_2-sintered SYT70a is phase-pure, whereas the H_2-sintered SYT70b contains a secondary Ti-rich phase ($SrTi_{10.7\pm0.2}O_{23-\delta}$).
(ii) The electrical conductivity of H_2-sintered SYT is high under reducing conditions (Fig. 10).
(iii) The electrical conductivity is proportional to the donor content (Fig. 11).

4.3.3. Transition from ionic compensation to electronic compensation

For the air-sintered SYT, a post-reduction process can change the compensation mode from an ionic one to an electronic one. However, as discussed above, the transition involves slow cation diffusion, and its kinetics is hence highly temperature dependent. At typical measuring temperatures (700–1000 °C), such a transition is considered to be impossible due to the frozen-in cations. At such temperatures, the only mobile ionic defects are the oxide ions. Oxygen is released from the SYT lattice, producing oxygen vacancies and conduction electrons according to

$$O_O^{\times} = V_O^{\bullet\bullet} + 2e' + \tfrac{1}{2}O_2(g) \quad (5)$$

Furthermore, even the oxide ions can only move slowly, which explains the observed ever-increasing electrical conductivity when the air-sintered SYT samples were measured at 910 °C under reducing conditions (Fig. 8). The reduction kinetics is determined by the bulk diffusion of oxide ions and is thus closely related to the microstructure. Porous and fine-grained materials should show much faster kinetics than dense and coarse-grained materials due to shorter diffusion lengths. The observed faster reduction kinetics for the stoichiometric compositions than for the A-site deficient compositions (Fig. 8) can, therefore, be attributed to their microstructural difference (Fig. 2).

The relatively low electrical conductivity (~1 S/cm) attainable by post-reduction of air-sintered SYT at about 900 °C indicates the limited contribution of electrons according to Eq. (5) to the electron density. Therefore, in order to achieve fast cation diffusion kinetics and hence a complete transition of the compensation mode for the air-sintered SYT, a high-temperature post-reduction process is apparently necessary. Within a fixed period of reduction time, the completeness of the transition is then dependent on the reduction temperature, as shown in Fig. 12. The electrical conductivity of samples directly sintered in Ar/4% H_2 at 1400 °C is also included in this figure. A general trend can be easily seen, i.e., higher reduction temperature leads to higher electrical conductivity no matter whether the reduction process is applied during or after the sintering process. It should be noted that the electrical conductivity also depends on the sample density, which in turn depends on the reduction temperature. In the present work, however, sample density (as indicated in Fig. 12) is not the determining factor.

5. Conclusions

In yttrium-substituted $SrTiO_3$ ceramics with (Sr + Y)/Ti ≤ 1, Y^{3+} ions occupy the Sr sites and act as donor substituents. Depending on the heat treatment of the material, the positive charge from the donor substituent can be compensated either electronically (by the reduction of Ti^{4+} to Ti^{3+}) or ionically (by strontium vancancies). The oxygen partial pressure under which the material experiences the final high-temperature heat treatment determines the compensation mechanism. Air-sintered samples show ionic compensation, while H_2-sintered samples show electronic compensation. For air-sintered samples, a high-temperature post-reduction process is necessary to convert the compensation mechanism from an ionic to an electronic one. As determined by this defect chemistry, the microstructure and electrical conductivity of yttrium-substituted $SrTiO_3$ materials show an interesting dependence on the starting compositions and sintering or processing conditions, which have not been reported in previous studies on this material.

To obtain a single-phase and highly conductive yttrium-substituted $SrTiO_3$ material, e.g. as a candidate for a good SOFC anode, a starting composition with (Sr + Y)/Ti = 1 combined with a high-temperature (>1200 °C) heat treatment under reducing conditions is required.

Acknowledgments

This research was supported by a *Marie Curie International Fellowship* under contract no. MIF1-CT-2004-509999 within the 6th European Community Framework Programme. The authors thank Dr. D. Sebold (FZJ-IEF 1) for the SEM investigations and P. Lersch (FZJ-IEF 2) for the XRD measurements.

References

1. McIntosh, S. and Gorte, R. J., Direct hydrocarbon solid oxide fuel cells. *Chem. Rev.*, 2004, **104**, 4845–4865.
2. Malzbender, J., Wessel, E. and Steinbrech, R. W., Reduction and re-oxidation of anodes for solid oxide fuel cells. *Solid State Ionics*, 2005, **176**, 2201–2203.
3. Marina, O. A., Canfield, N. L. and Stevenson, J. W., Thermal, electrical, and electrocatalytical properties of lanthanum-doped strontium titanate. *Solid State Ionics*, 2002, **149**, 21–28.
4. Hui, S. Q. and Petric, A., Electrical properties of yttrium-doped strontium titanate under reducing conditions. *J. Electrochem. Soc.*, 2002, **149**, J1–J10.
5. Makovec, D. and Drofenik, M., Microstructural changes during the reduction/reoxidation process in donor-doped $BaTiO_3$ ceramics. *J. Am. Ceram. Soc.*, 2000, **83**, 2593–2599.
6. Chan, H. M., Harmer, M. P. and Smyth, D. M., Compensating defects in highly donor-doped $BaTiO_3$. *J. Am. Ceram. Soc.*, 1986, **69**, 507–510.
7. Pechini, M.P., Method of preparing lead and alkaline earth titanates and niobates and coating method using the same to form a capacitor, U.S. Patent No. 3,330,697, 11 July 1967.
8. Dong, C., *User's Manual for PowderX*. Institute of Physics, Chinese Academy of Science, Beijing, 1998.
9. Boultif, A. and Louer, D., Indexing of powder diffraction patterns for low-symmetry lattices by the successive dichotomy method. *J. Appl. Cryst.*, 1991, **24**, 987–993.
10. McCarthy, G. J., White, W. B. and Roy, R., Phase equilibria in the 1375 °C isotherm of the system Sr–Ti–O. *J. Am. Ceram. Soc.*, 1969, **52**, 463–467.

11. Hessen, B., Sunshine, S. A. and Siegrist, T., New reduced ternary titanates from borate fluxes. *J. Solid State Chem.*, 1991, **94**, 306–312.
12. Fu, Q. X., Tietz, F. and Stöver, D., Electrical conductivity and redox behaviour of yttrium-substituted SrTiO3: dependence on preparation and processing procedures. In *Proceedings of the International Symposium on Solid Oxide Fuel Cells IX (SOFC-IX)*, ed. S. C. Singhal and J. Mizusaki, 2005, pp. 1417–1428.
13. Balachandran, U. and Eror, N. G., Electrical conductivity in strontium titanate. *J. Solid State Chem.*, 1981, **39**, 351–359.
14. Tsur, Y., Dunbar, T. D. and Randall, C. A., Crystal and defect chemistry of rare earth cations in $BaTiO_3$. *J. Electroceram.*, 2001, **7**, 25–34.
15. Xue, L. A., Chen, Y. and Brook, R. J., Influence of ionic radii on the incorporation of trivalent dopants into $BaTiO_3$. *Mater. Sci. Eng. B*, 1988, **1**, 193–201.
16. Zhi, J., Chen, A., Zhi, Y., Vilarinho, P. M. and Baptista, J. L., Incorporation of yttrium in barium titanate ceramics. *J. Am. Ceram. Soc.*, 1999, **82**, 1345–1348.
17. Makovec, D., Samardžija, Z. and Drofenik, M., Solid solubility of holmium, yttrium, and dysprosium in $BaTiO_3$. *J. Am. Ceram. Soc.*, 2004, **87**, 1324–1329.
18. Jeong, J. H., Park, M. G. and Han, Y. H., Defect chemistry of Y doped $BaTiO_3$. *J. Electroceram.*, 2004, **13**, 805–809.
19. Shannon, R. D., Revised effective ionic radii and systematic studies of interatomic distances in halides and chalcogenides. *Acta Cryst. A*, 1976, **32**, 751–767.
20. Eror, N. G. and Balachandran, U., Self-compensation in lanthanum-doped strontium titanate. *J. Solid State Chem.*, 1981, **40**, 85–91.
21. Balachandran, U. and Eror, N. G., Electrical conductivity in lanthanum-doped strontium titanate. *J. Electrochem. Soc.*, 1982, **129**, 1021–1026.
22. Flandermeyer, B. F., Agarwal, A. K., Anderson, H. U. and Nasrallah, M. M., Oxidation–reduction behaviour of La-doped $SrTiO_3$. *J. Mater. Sci.*, 1984, **19**, 2593–2598.
23. Moos, R. and Härdtl, K. H., Defect chemistry of donor-doped and undoped strontium titanate ceramics between 1000 and 1400 °C. *J. Am. Ceram. Soc.*, 1997, **80**, 2549–2562.
24. Moos, R., Bischoff, T., Menesklou, W. and Härdtl, K. H., Solubility of lanthanum in strontium titanate in oxygen-rich atmospheres. *J. Mater. Sci.*, 1997, **32**, 4247–4252.
25. Kröger, F. A. and Vink, H. J., *Solid State Physics*, *Vol. 3*, ed. F. Seitz and D. Turnbull. Academic Press, New York, 1956, p. 307.
26. Wernicke, R., Kinetics of equilibrium restoration in barium titanate ceramics. *Philips Res. Rep.*, 1976, **31**, 526–543.
27. Wernicke, R., Influence of kinetic processes on the electrical conductivity of donor-doped $BaTiO_3$ ceramics. *Phys. Stat. Sol. (a)*, 1978, **47**, 139–144.
28. Smyth, D. M., *Properties and Applications of Perovskite-Type Oxides*, ed. L. G. Tejuca and J. L. G. Fierro. New York, 1993, p. 47 [Chapter 3].
29. Morrison, F. D., Coats, A. M., Sinclair, D. C. and West, A. R., Charge compensation mechanisms in La-doped $BaTiO_3$. *J. Electroceram.*, 2001, **6**, 219–232.
30. Smyth, D. M., The defect chemistry of donor-doped $BaTiO_3$: a rebuttal. *J. Electroceram.*, 2002, **9**, 179–186.
31. Yoo, H.-I. and Lee, C.-E., Two-fold diffusion kinetics of oxygen re-equilibration in donor-doped $BaTiO_3$. *J. Am. Ceram. Soc.*, 2005, **88**, 617–623.
32. Nowotny, J. and Rekas, M., Defect structure, electrical properties and transport in barium titanate. VII. Chemical diffusion in Nb-doped $BaTiO_3$. *Ceram. Int.*, 1994, **20**, 265–275.
33. Garcia-Verduch, A. and Lindner, R., Selbstdiffusion in Bariummetatitanat. *Ark. Kemi*, 1953, **5**, 313–316.
34. Kiessling, U., Claus, J., Borchardt, G., Weber, S. and Scherrer, S., Oxygen tracer diffusion in lanthanum-doped single-crystal strontium titanate. *J. Am. Ceram. Soc.*, 1994, **77**, 2188–2190.
35. Claus, J., Leonhardt, M. and Maier, J., Tracer diffusion and chemical diffusion of oxygen in acceptor doped $SrTiO_3$. *J. Phys. Chem. Solids*, 2000, **61**, 1199–1207.
36. Balachandran, U. and Eror, N. G., Solubility of lanthanum in strontium titanate. *J. Am. Ceram. Soc.*, 1981, **64**, C75–C76.
37. Drofenik, M., Oxygen partial pressure and grain growth in donor-doped $BaTiO_3$. *J. Am. Ceram. Soc.*, 1987, **70**, 311–314.
38. Drofenik, M., Makovec, D., Zajc, I. and Langhammer, H. T., Anomalous grain growth in donor-doped barium titanate with excess barium oxide. *J. Am. Ceram. Soc.*, 2002, **85**, 653–660.
39. Burn, I. and Neirman, S., Dielectric properties of donor-doped polycrystalline $SrTiO_3$. *J. Mater. Sci.*, 1982, **17**, 3510–3524.
40. Yamamoto, T. and Sakuma, T., Abnormal grain growth of $BaTiO_3$ with small cation nonstoichiometry. *Mater. Sci. Forum*, 1996, **204–206**, 491–496.
41. Cho, Y. K., Kang, S.-J. L. and Yoon, D. Y., Dependence of grain growth and grain-boundary structure on the Ba/Ti ratio in $BaTiO_3$. *J. Am. Ceram. Soc.*, 2004, **87**, 119–124.